Tellus (1978), *30*, 436–448

On the dynamics and climatology of surface flow over the Equatorial oceans

By STEFAN HASTENRATH and PETER LAMB[1], *The University of Wisconsin, Dept. of Meteorology, 1225 West Dayton Street, Madison, Wisconsin 53706, U.S.A.*

(Manuscript received August 1, 1977; in final form February 14, 1978)

ABSTRACT

The surface circulation over the Equatorial Atlantic and Eastern Pacific is investigated using 60-year average ship data with a one-degree square resolution. At the height of the Northern summer, a zonally oriented speed maximum extends across the Eastern part of the oceans at about 4–5 N, near where the cross-equatorial flow recurves from Southeast to Southwest. This separates a band of strong divergence immediately to the North of the Equator from the convergence belt further poleward. Strongest convergence occurs about 350 km South of the confluence between Northern and Southern Hemisphere trades, and within a region of high directional steadiness of wind. A negative wind stress curl induces upwelling and low sea surface temperature immediately South of the Equator, and downwelling to the North.

In most of the Northeast trades and the Southeast trades of the Southern Hemisphere during July–August, frictional energy dissipation not offset by cross-isobaric flow produces a gradual slowing of the current and downstream convergence. As the Southern Hemisphere trades flow North from the Equator over the Eastern part of the oceans, the Coriolis acceleration increases acting to the right, enhancing the cross-isobaric angle and resulting in net kinetic energy generation, the aforementioned speed maximum and attendant zone of strong divergence. Continuation of this Coriolis effect recurves the flow from Southeast to Southwest, which further downstream diminishes the cross-isobaric angle, thus impairing kinetic energy generation and resulting in a band of maximum convergence. A positive relation is found between the latitude of the discontinuity separating Northern and Southern Hemisphere trades and the latitude and intensity of the zonally oriented convergence/divergence bands, both seasonally and on a year-to-year basis.

1. Introduction

An important and well-publicized component of the general circulation of the atmosphere has come to be termed the "Intertropical Convergence Zone" (ITCZ). The name ITCZ should strictly be applied only to the zone of maximum convergence in the near-equatorial wind field. Use of this term in relation to the Equatorial oceans, however, has often considered the convergence maximum to coincide with, and even be synonymous with, the confluence between Northern and Southern hemisphere trades, the zone of maximum sea surface temperature (SST), the surface pressure trough, and bands of maximum cloudiness and rainfall (review in Ramage, 1974). The above interpretation has sometimes included the suggestion that the ITCZ is the locus of cloud clusters associated with Westward propagating wave disturbances (review in Lockwood, 1974, pp. 89–93). On the other hand, Sadler (1964) and Ramage (1974) found the near-equatorial zone of minimum pressure to be overlain by clear skies, suggesting that maximum convergence, cloudiness, and rainfall occur elsewhere. Furthermore, Saddler (1975) has noted that the mean monthly cloud zone does not coincide with the tracks of migratory vortices, and that synoptic-scale disturbances are not important in producing the maximum cloud zones. Some disagreement therefore exists over the structure of this

[1] Present affiliation: The University of Adelaide, Geography Dept., G.P.O. Box 498, Adelaide, South Australia 5001.

complex of near-equatorial atmospheric and oceanic features.

The present paper utilizes a large set of observational data to investigate the 60-year (1911–70) mean patterns of surface pressure, wind, divergence, sea surface temperature, total cloudiness, and precipitation frequency for the Atlantic and Eastern Pacific oceans between 20 N and 10 S. Emphasis is placed on identifying the spatial relationships between contemporary patterns of different parameters, and their geographical and seasonal variations. Limited study is also made of the dynamics of the most distinctive circulation features.

A one-degree square spatial resolution is used here. Earlier marine atlases do include the ocean areas studied in the present paper (e.g. Koninklijk Nederlands Meteorologisch Instituut, 1918–31; U.S. Weather Bureau, 1938; Mintz and Dean, 1952; U.S. Navy 1955–59; Atkinson and Sadler, 1970); however, their coarse spatial resolution (two- or five-degree squares) provides only a smoothed picture of the circulation, while inconsistencies in resolution, data coverage, and presentation format have hampered the comparison of patterns for different parameters. The present paper identifies small-scale features that have escaped the coarse mesh of earlier charts, including the very recent work of Romanov and Romanova (1976), but which appear essential for the understanding of low latitude circulations.

2. Observational basis

Ship data for the period 1911–72 were obtained on magnetic tape from the U.S. National Climatic Center at Asheville, N.C. These were in the form of individual monthly averages of various meterological parameters for one-degree latitude by one-degree longitude squares in the Tropical Atlantic and the Eastern Pacific. Full details of this data set are given in Hastenrath and Lamb (1977a). Of interest here are 60-year averages for the fields of wind, pressure, SST, cloudiness and precipitation frequency between 20 N–10 S. Fields of derived quantities, such as divergence and directional steadiness of wind, were also obtained using a one-degree square resolution.

Some 3.5 million sets of observations were available for the above area. Data were subject to quality control checks when taped, with values beyond physically reasonable limits being excluded. Wind speed was converted from original Beaufort estimates. Verploegh (1967) found wind force data obtained by simple observation to be as accurate as ship's wind measurements. Observations of atmospheric pressure aboard ship are less reliable than those made at land stations. Ship-board measurements of SST are likely to be overestimations (e.g. Saur, 1963; Ramage et al., 1972); because of the uncertainties of these errors, however, no corrections were applied. The large-scale pattern of SST considered here should be little affected.

An atlas with a two-degree square spatial resolution exists for the Indian Ocean (Koninklijk Nederlands Meteorologisch Instituut, 1952).

3. Atmospheric circulation patterns

The July–August patterns include a number of characteristics not apparent in other months, and are therefore presented in some detail in Fig. 1. Prominent features not revealed by earlier maps are as follows: a zonally oriented speed maximum extends over the Eastern part of both oceans, near the latitude where the cross-equatorial flow recurves from Southeast to Southwest; this broadly separates a band of distinct divergence immediately to the North of the Equator from the convergence belt further poleward; strongest convergence is situated well to the South of the surface confluence axis, and within a region of high directional steadiness of wind. The latitudinal arrangement of near-equatorial circulation, weather, and oceanic features during July–August is illustrated in more detail in the meridional profiles in Figs. 2–4.

3.1. *West African sector*

In the Eastern Atlantic, Fig. 2, a band of low SST is prominent immediately to the South of the Equator; a flat SST maximum extends between 5 and 14 N. This approximately underlays a broad trough of low pressure. The resultant wind discontinuity essentially coincides with the axis of minimum pressure. A maximum of both resultant and scalar wind speed is apparent around 4–5 N. Jordan's (1951) July charts of resultant wind components show some indication of this feature, while Flohn (1970) noted a maximum of scalar

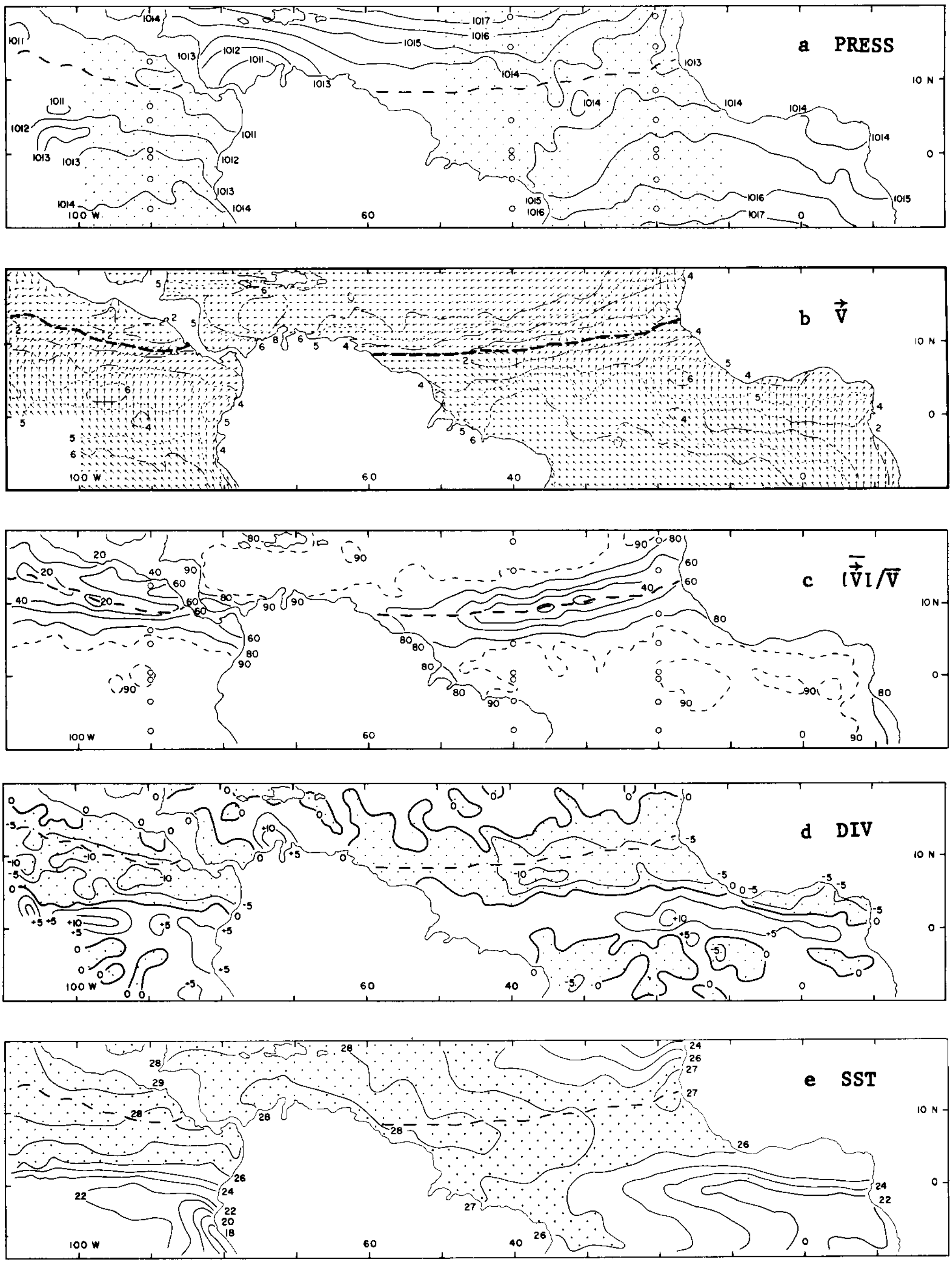

Fig. 1. Surface circulation over the Equatorial Atlantic and Eastern Pacific, July–August, 1911–70. a. pressure PRESS (mb); ocean areas represented in Figs. 2–8 are indicated by dot roster, and latitudes of vector diagrams in Figs. 6–8 by open circles; b. resultant wind direction and speed $\vec{V}$ (m s^{-1}); c. steadiness of wind $|\vec{V}|/\bar{V}$ (%), latitudes of vector diagrams in Figs. 6–8 are marked by open circles; d. divergence DIV (10^{-6} s^{-1}), with convergence shaded; e. sea surface temperature SST (°C), with areas above 26°C shaded. Position of resultant confluence axis is shown as heavy broken line in maps a, b, c, d, and e.

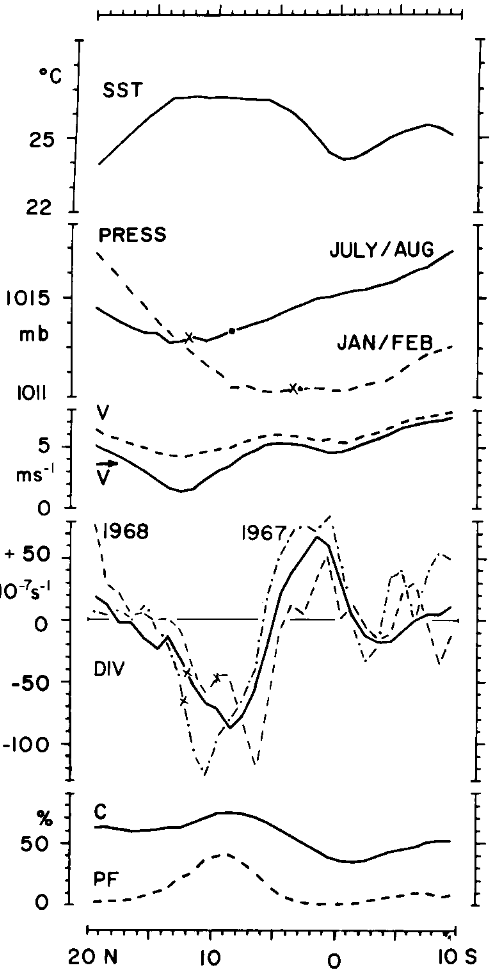

Fig. 2. Eastern Equatorial Atlantic, 10–30 W, July–August 1911–70. Meridional profiles of selected elements: sea surface temperature, SST; sea level pressure PRESS, with January–February values plotted as broken line, and position of surface confluence axis and maximum convergence indicated by crosses and dots, respectively; resultant $\vec{V}$, solid, and scalar wind speed, V, broken line; divergence, DIV, with values for July–August of 1968 (dry) and 1967 (wet) entered as broken and dash-dotted lines; total cloudiness C, solid, and precipitation frequency PF, broken line.

wind speed at a similar latitude in the 0–20 W sector during July. A speed minimum is found near the wind discontinuity. Comparison of resultant and scalar wind speed reveals high directional steadiness within most of the clockwise turning cross-equatorial monsoon flow as well as in the upstream portion of the Northeast trades. The vicinity of the wind discontinuity is characterized by low steadiness values. Fig. 2 also identifies a band of pronounced divergence between about 1 S and 5 N, with a wider belt of convergence lying immediately to the North. The convergence maximum stays 3–4 degrees of latitude to the South of the wind discontinuity. The maximum of precipitation frequency is displaced slightly to the North of—or downstream from—the convergence maximum. The cloudiness maximum also extends further North than the convergence and rainfall maxima. Rainfall and cloudiness maxima in this sector also occurred to the south of the surface confluence line during the GATE experiment (Estoque and Douglas, 1978).

3.2. *Eastern Pacific*

For the Eastern Equatorial Pacific, Fig. 3 illustrates conditions similar to the Eastern Atlantic, the major differences being as follows: SST increases to the northernmost portion of the transect; the maxima of precipitation frequency, and even more so of cloudiness, are displaced to the South of the convergence maximum, which in turn stays well to the South of the wind discontinuity as in the Atlantic. The southward displacement of the largest cloudiness from the convergence maximum may result from the clockwise-turning flow from the Southern Hemisphere being overlain by northeasterlies, which would tend to spread cloud tops southward. The clockwise turning cross-equatorial flow over the Eastern Pacific extends only to about 1 km at the Equator (Hastenrath, 1977a). The cross-equatorial flow over the Eastern Atlantic is less shallow (Hastenrath and Lamb, 1977b).

Figs. 1–3 identified zonally oriented tongues of cold water immediately to the South of the Atlantic and Pacific Equator. The horizontal advection of cold surface water from off the Southern Hemisphere continental West coasts by wind-driven ocean currents would serve to maintain this feature. However, a further atmosphere–ocean interaction mechanism may be involved. Over the Eastern part of the oceans during Northern summer (Fig. 1), negative vorticity occurs in a broad band extending on either side of the Equator; the curl of the wind stress has a similar pattern (Hasternrath and Lamb, 1977a). This wind stress pattern favors

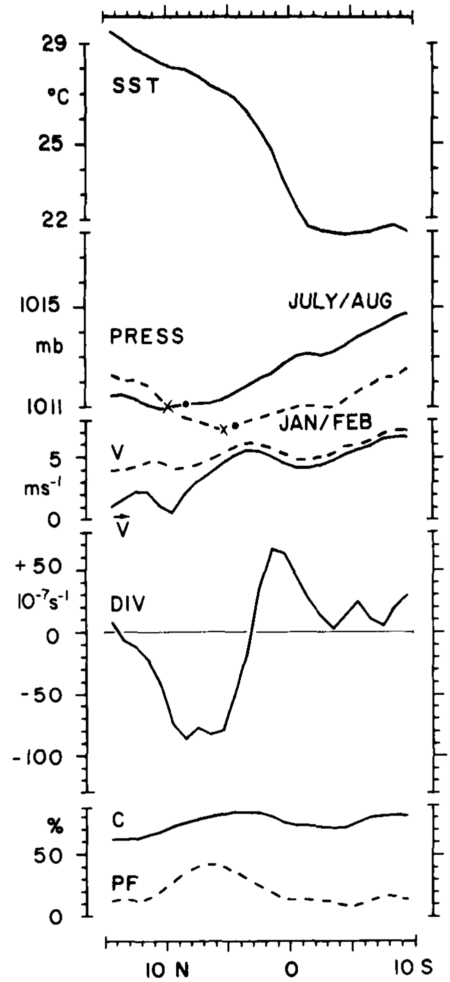

Fig. 3. Eastern Equatorial Pacific, 80–100 W, July–August 1911–70. Meridional profiles of selected elements. Symbols as in Fig. 2.

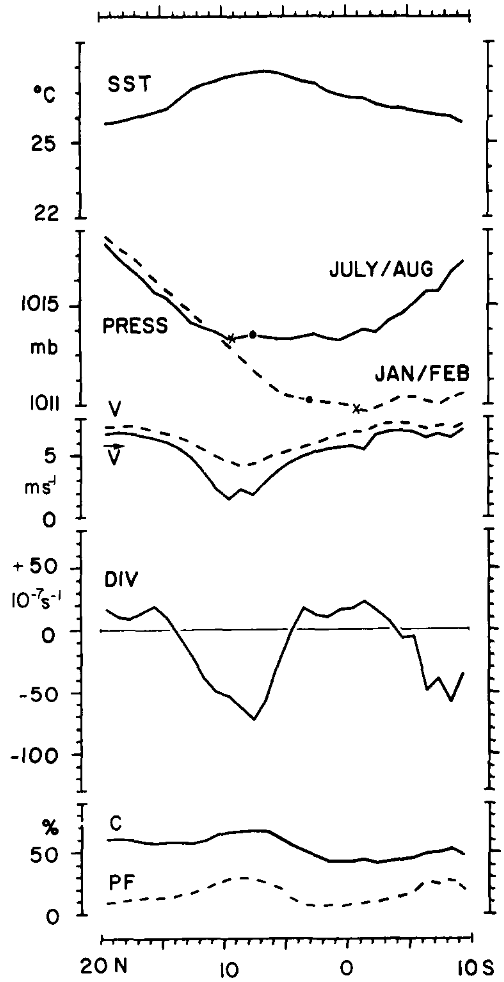

Fig. 4. Western Equatorial Atlantic, 30–50 W, July–August 1911–70. Meridional profiles of selected elements. Symbols as in Figs. 2–3.

oceanic upwelling in the Southern Hemisphere and downwelling in the Northern Hemisphere, with particularly large magnitudes near the Equator (Hantel, 1972). The possible importance of this mechanism is underlined by the steep meridional SST gradients across the Eastern Atlantic and Pacific Equator and the fact that both the negative wind stress curl and the cold water tongues are best developed in Northern summer (Hastenrath and Lamb, 1977a). Yet another mechanism of wind-induced vertical motion in the ocean has been proposed by Cromwell (1953). The possible role of this mechanism for the Eastern Atlantic and Pacific has been discussed by Hastenrath (1977b). The aforementioned SST pattern results in a marked hemisphere asymmetry of the oceanic heat budget (Hastenrath, 1977b).

3.3. *Brazil sector*

Fig. 4 portrays the atmospheric-oceanic conditions of the Western Equatorial Atlantic. The flat extrema of SST and pressure essentially coincide, and the kinematic axis—here in the form of an asymptotic confluence (Fig. 1)—is embedded in the pressure trough. Wind speed and directional steadiness decrease towards the confluence axis, with no development of a near-equatorial speed maximum as in the two foregoing sea areas.

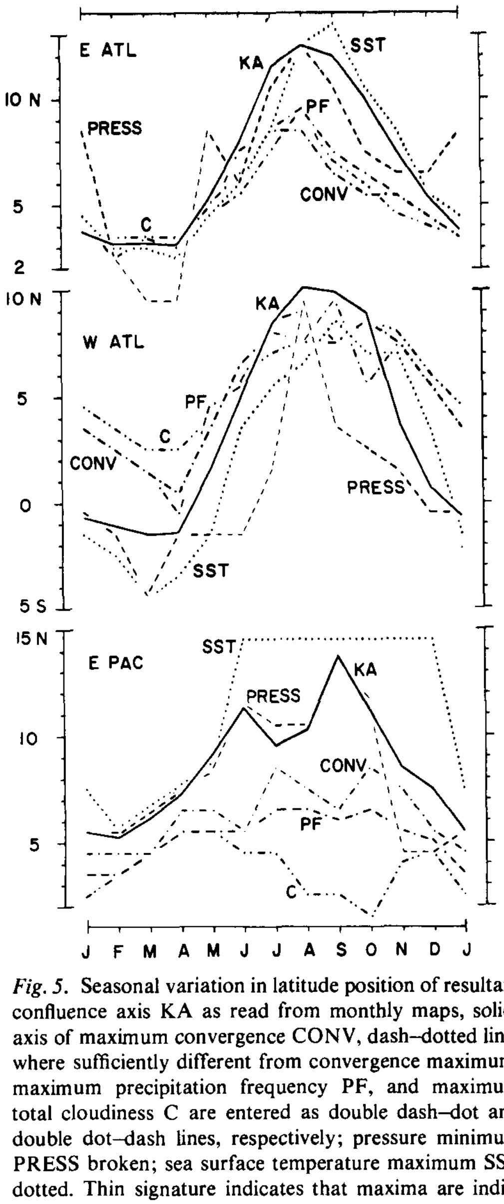

Fig. 5. Seasonal variation in latitude position of resultant confluence axis KA as read from monthly maps, solid; axis of maximum convergence CONV, dash–dotted line; where sufficiently different from convergence maximum, maximum precipitation frequency PF, and maximum total cloudiness C are entered as double dash–dot and double dot–dash lines, respectively; pressure minimum PRESS broken; sea surface temperature maximum SST dotted. Thin signature indicates that maxima are indistinct. Top Eastern Atlantic 10–30 W, middle Western Atlantic 30–50 W, bottom Eastern Pacific 80–100 W.

Strongest convergence is also located to the South of the kinematic axis, although the latitudinal separation is smaller than over the Eastern part of the oceans. As over the Eastern Atlantic, the maximum of precipitation frequency is found slightly to the North of—that is downstream from—the convergence maximum.

3.4. *Indian Ocean*

The summer monsoon current over the Indian Ocean (Koninklijk Nederlands Meteorologisch Instituut, 1952) shows no near-equatorial speed band; the areas of highest speed occur over the Arabian Sea and Bay of Bengal. The low-level cross-equatorial jet over the Western Indian Ocean (Findlater, 1974) has speed maxima on either side of the Equator. In contrast to the Eastern Atlantic and Pacific, a marked zonal component of the pressure gradient is characteristic North of the Equator, with a meridionally oriented ridge near 70 E.

4. Atmospheric-oceanic seasonal variations

Fig. 5 compares the latitudes of the confluence axis and the extrema of SST, pressure, convergence, precipitation frequency, and cloudiness, during the course of the year. All of these individual axes undergo a marked seasonal variation in latitude, but of greater interest are the variations in their collective spatial arrangement.

In the Eastern Atlantic, the SST and pressure extrema and confluence axis are in close proximity throughout the year. The convergence maximum is located equatorward of the confluence axis and pressure and SST extrema during most of the year, with the latitudinal separation becoming very large in Northern summer. Maxima of precipitation frequency and cloudiness nearly coincide with the convergence maximum during most of the year, but are displaced somewhat to the North in summer and fall.

In the Eastern Pacific, the SST maximum stays poleward of the confluence axis, this being most pronounced during the summer half year. The confluence axis and pressure minimum nearly coincide and undergo a double variation in the course of the year. The convergence maximum is found on the equatorward side of the confluence axis, again with a largest latitudinal separation during the summer half year. The maxima of precipitation frequency and particularly cloudiness tend to stay equatorward of the convergence maximum, with the greatest latitudinal separation occurring during the summer half year.

In the Western Atlantic, the SST maximum and pressure minimum tend to stay to the South of the confluence axis throughout most of the year. The convergence maximum, and the maxima of precipitation frequency and cloudiness, are located on the equatorward side of the confluence axis in Northern summer, and on its Northern side in winter.

Figs. 1–4 show that the bands of maximum convergence are largely located in regions of high wind steadiness, namely at values of about 70% over the Eastern Atlantic and 50% in the Western Atlantic, and around 80% over the Eastern Pacific; in the zone of the largest cloudiness over the Eastern Pacific, directional steadiness of wind is even around 90%. Low steadiness values in the vicinity of the confluence axis are in a region of lesser cloudiness. This detail not revealed by earlier atlas charts is interesting in relation to Sadler's (1975) contention that the mean monthly maximum cloud zone does not coincide with the tracks of migratory vortices, and that synoptic scale circulations are not important in producing the maximum cloud zone. It is noted, however, that surface observations are analyzed here and the displacement of "cloud clusters" may reflect conditions in higher layers.

5. Dynamics of July–August surface flow

5.1. *Theory and computations*

The equations of motion for large-scale (horizontal) climatic mean (steady-state) flow can be written in component form as

$$\frac{d\bar{u}}{dt} = \bar{u}\frac{\partial \bar{u}}{\partial x} + \bar{v}\frac{\partial \bar{u}}{\partial y} + \overline{u'\frac{\partial u'}{\partial x}} + \overline{v'\frac{\partial u'}{\partial y}}$$

$$= + f\bar{v} - \bar{\alpha}\frac{\partial \bar{p}}{\partial x} - \overline{\alpha'\frac{\partial p'}{\partial x}} + \bar{F}_x \tag{1a}$$

$$\frac{d\bar{v}}{dt} = \bar{u}\frac{\partial \bar{v}}{\partial x} + \bar{v}\frac{\partial \bar{v}}{\partial y} + \overline{u'\frac{\partial v'}{\partial x}} + \overline{v'\frac{\partial v'}{\partial y}}$$

$$= - f\bar{u} - \bar{\alpha}\frac{\partial \bar{p}}{\partial y} - \overline{\alpha'\frac{\partial p'}{\partial y}} + \bar{F}_y \tag{1b}$$

or in vector notation

$$\frac{d\vec{V}}{dt} = \bar{\vec{V}}\cdot\nabla\bar{\vec{V}} + \overline{\vec{V}'\cdot\nabla\vec{V}'}$$

$$= - f\vec{k}\times\bar{\vec{V}} - \bar{\alpha}\vec{\nabla}\bar{p} - \overline{\alpha'\vec{\nabla}p'} + \bar{\vec{F}} \tag{2}$$

Bars denote time-averages, taken here for July–August 1911–70, and primes departures from such averages. Following conventional notation, $\vec{V}$, u, v, $\vec{F}$, F_x, F_y, are the horizontal wind vector, its eastward and northward components, the frictional force per unit mass, and its components, respectively, a, p, f, and ∇ denote specific volume, pressure, Coriolis parameter and horizontal nabla-operator.

Data available for the present study permitted the direct evaluation of the first left-hand and first two right-hand terms of Eq. (2). These terms were evaluated in component form for each one-degree latitude strip of the three sub-areas considered in Section 3. Resultant and geostrophic wind vectors were also obtained for each one-degree zone. Derivatives in the zonal direction were computed as finite differences between the means of the Eastern and Western halves of each one-degree strip. Meridional derivatives relating to a given latitude band were computed as finite differences between average values for the contiguous one-degree strips to the North and South.

The terms in Eq. (2) containing primed quantities could not be evaluated directly. They were therefore assumed to be negligible, which allowed the friction vector $\bar{\vec{F}}$ to be obtained as the residual of Eq. (2). Figs. 6–8 present examples of friction vectors obtained using this method, together with the other acceleration vectors and those for the resultant and geostrophic winds, for locations where the directional steadiness of wind exceeds 60%. The vectors for a location with directional steadiness as low as 20% (9.5 N in Eastern Pacific) are included in the insert to Fig. 7 for comparison. In view of the predominant zonal uniformity within each sub-area (Fig. 1), the vector diagrams for successive latitude strips essentially represent the conditions along a streamline/trajectory.

Inconsistencies in the sets of acceleration vectors obtained by the above procedure could result from covariance in wind speed fluctuations making the primed terms on the left-hand side of Eqs. (1)–(2) non-zero, and from deficiencies in the temporal and spatial sampling of observations and the analysis procedures. How realistic the residual friction vectors in Figs. 6–8 are, thus indicates whether the above error sources unduly affected the patterns of forces produced. At locations of low directional steadiness of wind, as exemplified by the diagrams for 9.5 N in Fig. 7, the sets of forces obtained are

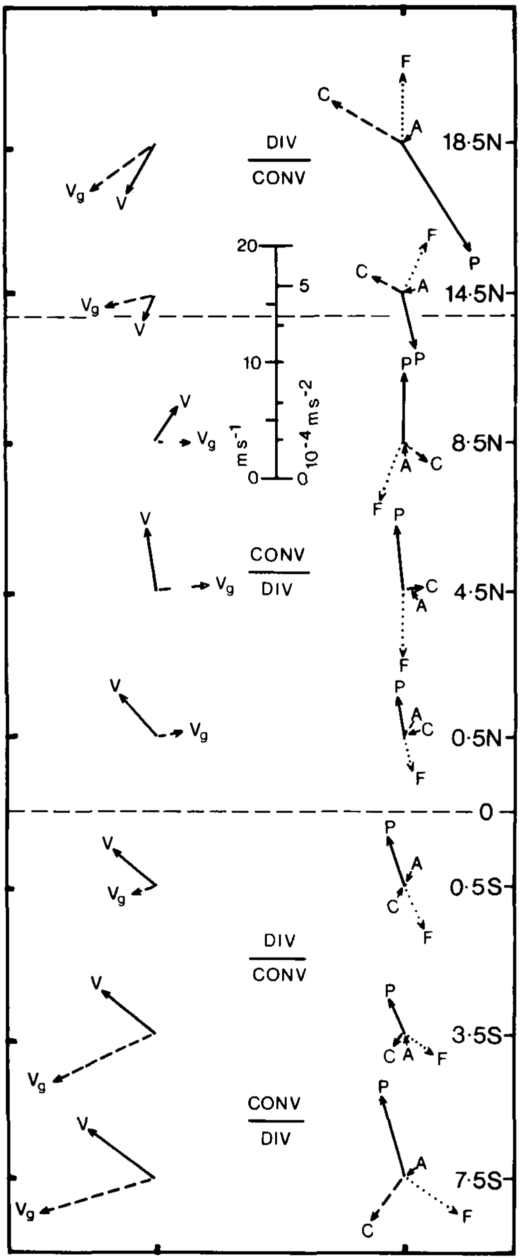

Fig. 6. Eastern Equatorial Atlantic, 10–30 W, July–August 1911–70. Dynamics of surface flow. Equator and latitude of resultant confluence axis are schematically entered as broken lines. Left: resultant wind V solid, and geostrophic wind vector V_g broken, see scale of m s^{-1}; very large values of V_g are plotted at one-third the regular scale, being denoted by a gap in the middle of the arrow; for 0.5 N and S only the direction of V_g is given. Right: pressure gradient acceleration $P = -\bar{\alpha}\nabla p$ solid, Coriolis acceleration $C = f\vec{V} \times \vec{k}$ broken, frictional force per unit mass F dotted, advective acceleration $A = \vec{V} \cdot \nabla \vec{V}$, see scale of m s^{-2}.

indeed not reasonable and are not considered in this study. Meaningful constellations of acceleration vectors were, however, produced for regions of high directional steadiness. As Figs. 6–8 indicate, the residual friction vectors are in general directed approximately opposite to the resultant wind vector; exact opposition is not even expected from theory. Furthermore, the magnitudes of the friction vectors were checked using two independent comparisons. For an average wind speed at ships' deck level of 7.5 m s^{-1}, Brümmer et al. (1975) found the frictional deceleration of the North Atlantic Trades at 10 N during ATEX to be 16.3 × 10^{-5} m s^{-2}. The frictional coefficient in Guldberg and Mohn's linear formulation $|\vec{F}| = k|\vec{V}|$ has been reported to have open ocean values of 1 to 3 × 10^{-5} s^{-1} (Gordon and Taylor, 1975); Brümmer et al.'s (1974) data would yield a figure of 2.3 × 10^{-5} s^{-1}. The wind speed and residual friction data in the present study yield values of frictional deceleration and k comparable in magnitude to those cited above.

If we assume the primed terms in Eq. (1a) to be negligible, this equation can be used to examine the influence of the pressure field on the recurvature of the Southeast Trades. At the latitude where the cross-equatorial flow recurves from Southeasterly to Southwesterly, Eq. (1a) has the following characteristics: the first left-hand term is zero, and the second left-hand term is positive; the last right-hand term is zero in a first approximation, and the first right-hand term is positive in the Northern and negative in the Southern Hemisphere. It follows that recurvature of the mean flow South of the Equator would require the second right-hand term to be positive, implying a pressure decrease towards the East. In contrast, the flow can recurve in the Northern Hemisphere with a zero, westward or very weak eastward directed pressure gradient.

5.2. *Eastern Pacific and West African sector of Atlantic*

Figs. 6–7 illustrate the variation of wind and acceleration vectors between significant parts of the cross-equatorial flow in these areas. For the Eastern Atlantic, pressure decreases from the

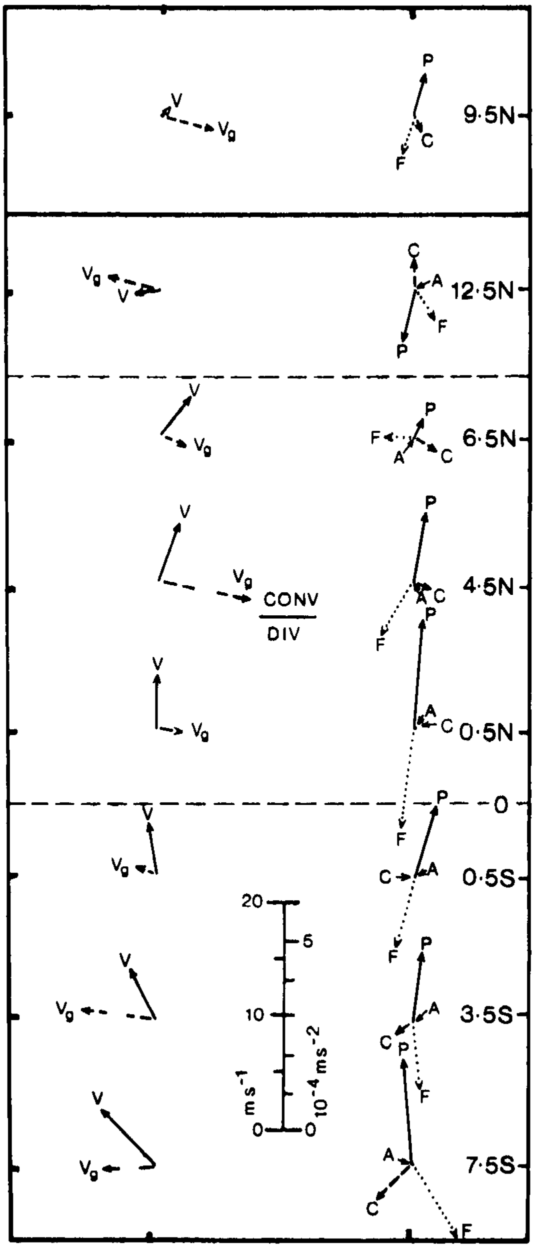

Fig. 7. Eastern Equatorial Pacific, 80–100 W, July–August 1911–70. Dynamics of surface flow. Symbols as in Figs. 6–7.

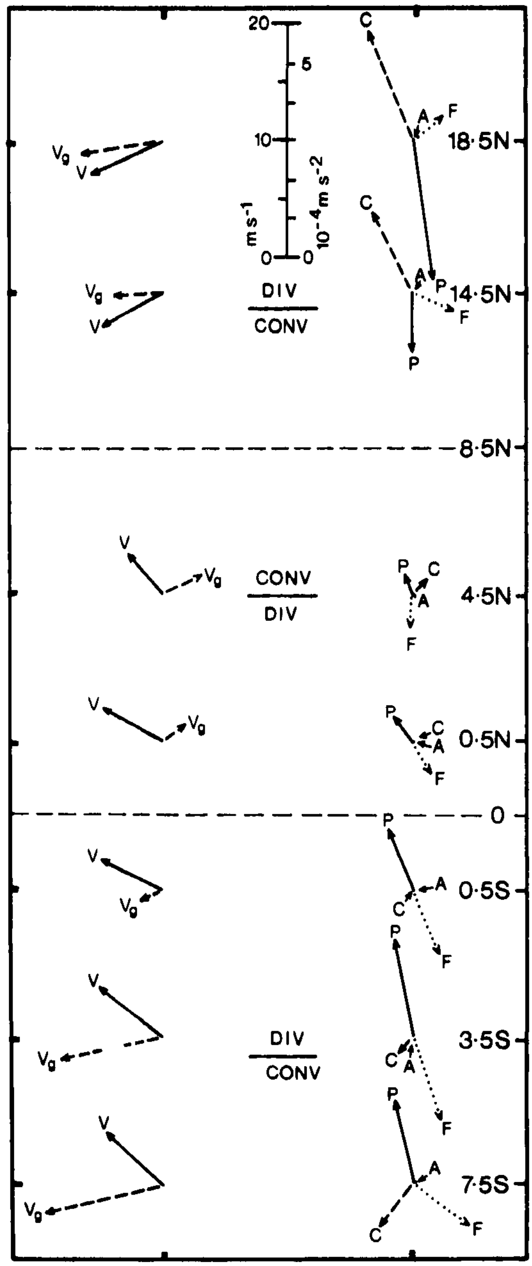

Fig. 8. Western Equatorial Atlantic, 30–50 W, July–August 1911–70. Dynamics of surface flow. Symbols as in Fig. 6.

Southern Hemisphere across the Equator to a minimum at 9–14 N (Fig. 2). In the Southeasterlies of the Southern Hemisphere, frictional energy dissipation not offset by cross-isobaric generation seems to produce a gradual slowing of the current, the direction of which remains essentially unchanged (Figs. 1, 2, and 6). This is consistent with the modest convergence South of the Equator in Figs. 1, 2, and 6. Proceeding North from the Equator, the Coriolis force increases and acts in a direction opposite to the Southern Hemisphere, individual (or advective) accelerations towards the right of the flow gain importance, and the cross-isobaric angle is enhanced, favoring kinetic energy generation (Fig. 6). As a consequence, the current speeds up and bends to the right, recurving to W of S at about 5 N (Fig. 1). Speed increases from the Equator to about this latitude (Figs. 1–2). Romanov and Romanova (1976) noted a similar recurvature latitude, but did not detect the associated speed maximum. The eastward turning of the wind continues with further movement North, reducing the cross-isobaric flow component to the extent that the kinetic energy generation apparently does not offset frictional dissipation (Fig. 6). The current slows down from the recurvature latitude to the flow discontinuity. For the concomitant zonally oriented divergence and convergence bands see Figs. 1, 2 and 6.

The Northeast trades slow down towards the kinematic discontinuity, presumably also because frictional dissipation is not altogether compensated by generation of kinetic energy through cross-isobaric flow. This leads to convergence on the poleward side of the kinematic discontinuity/pressure trough (Figs. 1, 2, and 6).

The resultant wind is everywhere weaker than the geostrophic wind; the resultant direction is to the right of the geostrophic wind in the Southern Hemisphere and to the left in the Northern Hemisphere (Fig. 6). Away from the immediate vicinity of the Equator, the difference between resultant and geostrophic vectors appears due to the substantial frictional deceleration in the Northeast trades and clockwise turning cross-equatorial flow. The ageostrophy close to the Equator is related to the Coriolis acceleration being, by definition, near zero.

Fig. 7 illustrates the latitudinal variation of wind and acceleration vectors in the Eastern Pacific. This reveals flow characteristics and mechanisms comparable to those of the Eastern Atlantic, both for the cross-equatorial current to the South of the kinematic discontinuity/pressure trough, and the Northeast trades to the North.

Long-term mean monthly charts (Hastenrath and Lamb, 1977a) show, for the Eastern Atlantic and Pacific on a month-to-month basis, a positive relation between the latitude of the surface flow discontinuity, the intensity of the associated convergence belt, and the width and strength of the divergence band immediately to the North of the Equator. The Eastern Atlantic wind and divergence fields for 2 years with highly contrasting Subsaharan rainy seasons suggest this relationship may also exist on a year-to-year basis. Prominent features of the extreme drought year 1968 as compared to 1967, a wet year in Western Subsaharan areas (Lamb, 1978), are (Fig. 2) a more equatorward position of the surface wind discontinuity, a southward displacement and weakening of the convergence band, and a weak development of the divergence belt immediately to the North of the Equator.

The foregoing relationship results from the already noted dependence of the divergence/convergence pattern on the speed maximum, which in turn is dependent on the lattitude of the flow discontinuity. If the flow discontinuity and its attendant convergence zone are relatively close to the Equator, then the mechanism offered above to account for the speed maximum would have insufficient space to operate fully. This would restrict the development of the speed maximum, and therefore the divergence belt immediately North of the Equator. The windspeed decrease from the maximum to the discontinuity would also be reduced, which may weaken the convergence band, and place the convergence maximum close to the flow discontinuity rather than further South. In the extreme case of the 60-year average January and February (Hastenrath and Lamb, 1977a), these processes produce a complete elimination of the speed maximum and concomitant divergence belt, and a coincidence of the convergence maximum and confluence axis (Figs. 2 and 3). The less extreme comparison of July–August 1967 and 1968 made above, revealed variations in the development of features rather than their elimination (Fig. 2).

5.3. *Indian Ocean*

In remarkable contrast to the Eastern Atlantic and Pacific patterns identified in Section 3, the July–August monsoon flow East of 70 E recurves to Southwesterly prior to the Equator being crossed, and does not possess a near-equatorial speed maximum (Koninklijk Nederlands Meteorologisch Instituut, 1952). The strong eastward directed pressure gradient over the Indian Ocean is fundamental to these flow differences; using Eq. (1a), this was found to be a necessary condition for recurvature South of the Equator. An increase in speed North of the recurvature into the Arabian Sea and Bay of Bengal results from mechanisms similar to those in the Eastern Atlantic and Pacific. However, the continued eastward turning of the wind over the Northern Indian Ocean East of about 70 E does not involve decreased kinetic energy generation, because strong cross-isobaric flow is ensured by the zonally asymmetric pressure configuration. The orientation of isobars over the Western Arabian Sea is unfavorable for cross-isobaric flow, but a speed maximum does occur, albeit well away from the Equator.

Gordon and Taylor (1975) computed trajectories and divergence for the July surface flow over the Indian Ocean, using meridional pressure profiles and winds at an initial latitude given by Koninklijk Nederlands Meteorologisch Instituut (1952). Zonal pressure gradients, however, were neglected. Their trajectories do not recurve South of the Equator, presumably as a consequence of the assumed zonal symmetry of isobars. The associated divergence pattern bears some resemblance to the one computed by Hantel (1970) on the basis of actual wind charts also taken from the Dutch Atlas. Over the Western Arabian Sea, where surface speed maxima on either side of the Equator are well developed, Hantel's charts show convergence bands around 4 S and North of 18 N, the former in similarity with conditions over the Eastern Atlantic and Eastern Pacific.

5.4. *Brazil sector of Atlantic*

The flow dynamics in the realm of the asymptotic trade wind confluence of the Western Atlantic are illustrated in Fig. 8. Pressure decreases from the Southern Hemisphere across the Equator to a minimum near 8 N (Figs. 1 and 4), as characterized the other sub-areas considered in Figs. 2–3 and 6–7. The relation between the resultant and geostrophic wind vectors in Fig. 8 is similar to that described for Figs. 6–7. In similarity to the Eastern Atlantic and Pacific, the Northeast trades slow down as the confluence axis is approached, due to frictional dissipation of kinetic energy not being replaced by cross-isobaric generation. The Southeast trades to the South of the Equator also behave like those of the other sub-areas, in that speed decreases down-stream conceivably because frictional dissipation exceeds the kinetic energy generation by cross-isobaric flow. The Brazilian coast may be a contributing factor here (Fig. 1). This speed pattern is consistent with the convergence South of about 4 S in Figs. 1 and 4. A band of moderate divergence straddles the Equator in the Western Atlantic (Figs. 1 and 4), whereas in the Eastern Atlantic and Pacific most of a comparable zone of divergence lies immediately North of the Equator (Figs. 1–3). Figs. 1 and 4 show little, if any, evidence of the Western Atlantic divergence belt coinciding with a downstream increase in wind speed, unlike the other sub-areas. Instead, it seems to result from the flow in the Western Atlantic sector being diffluent (Fig. 1), which may partly stem from the current in the Eastern half of the sector bending to the right with movement from 5 S to 5 N. A reduction in the Coriolis acceleration to the left prior to the Equator, and its subsequent increase to the right, would seem to be involved. The pressure gradient is very slack from the divergence band to the confluence axis, which curtails the generation of kinetic energy, and is manifest in terms of a downstream speed decrease and convergence (Figs. 1 and 4). The importance of the meridional pressure gradients on either side of the confluence axis for the kinetic energy imbalance and convergence pattern is underlined by the pressure profiles in Fig. 4: the convergence maximum switches from the Southern (summer) to Northern (winter) side of the confluence axis, as the Northern meridional pressure gradient becomes the steepest.

6. Conclusions

Understanding of the mechanisms controlling the surface circulation over Equatorial oceans has been hampered by the course spatial resolution of the climatic mean data hitherto available. Ramage (1974) has summarized, and taken exception to, the widely accepted view of a coincidence of the zones of maximum SST, convergence, and rainfall-cloudiness, and the baric trough and kinematic discontinuity. This complex has been commonly referred to as the ITCZ.

The present study has shown the confluence axis to be embedded in a flat low pressure trough. Over the Eastern Pacific, the SST maximum stays to the North of the confluence throughout the year, whereas they are in close proximity in the Atlantic. The convergence maximum lies to the South of the confluence axis and SST maximum throughout the year in the Eastern Pacific, and during most of the year in the Atlantic. In the Indian Ocean, the SST maximum is generally situated North of the convergence maximum (Koninklijk Nederlands Meteorologisch Instituut, 1952; Hantel, 1970). By way of comparison it is noted that numerical simulation experiments (review in Ramage, 1974) have produced near-equatorial convergence and rain bands coincident with a prescribed SST maximum.

The available observational data limited the dynamics section to study of the basic flow. This is unsatisfactory in regions of low wind steadiness, where the perturbation component of the flow is relatively important. However, the zonally oriented convergence and divergence bands within the cross-equatorial flow from the Southern Hemisphere are characterized by very high directional steadiness of wind. The origin of this prominent vergence pattern is at least qualitatively understood in terms of the basic flow. The development of the zones of convergence/divergence is related to the poleward shift of the kinematic discontinuity, both in terms of the seasonal march and the behavior of individual extreme years.

7. Acknowledgements

This study was supported by the Office of Climate Dynamics of The National Science Foundation. Discussions with M. Hantel and J. Young are gratefully acknowledged.

REFERENCES

Atkinson, G. and Sadler, J. C. 1970. Mean cloudiness and gradient-level wind charts over the tropics. USAF, Air Weather Service Technical Report No. 215.

Brümmer, B., Augstein, E. and Riehl, H. 1974. On the low-level wind structure in the Atlantic trade. *Quart. J. Roy. Meteor. Soc. 100*, 109–121.

Cromwell, T. 1953. Circulation in a meridional plane in the Central Equatorial Pacific. *J. Mar. Res. 12*, 196–213.

Estoque, M. A. and Douglas, M. 1978. Structure of the intertropical convergence zone of the GATE area. *Tellus 30*, 55–61.

Findlater, J. 1974. The low-level cross-equatorial air current of the Western Indian Ocean during the Northern Summer. *Weather 29*, 411–416.

Flohn, H. 1970. Investigations of equatorial upwelling and its climatic role. In: *Studies of Physical Oceanography, tribute to Georg Wüst on his 80th Birthday* (ed. A. C. Gordon), Vol. 1. New York and London: Gordon and Breach, pp. 93–102.

Gordon, A. H. and Taylor, R. C. 1975. *Computations of surface layer air parcel trajectories, and weather, in the oceanic tropics*. International Indian Ocean Expedition, Meteor. Monogra. No. 7. University Press of Hawaii, 112 pp.

Hastenrath, S. 1977a. On the upper-air circulation over the equatorial Americas. *Archiv. Meteorol. Geophys. Bioklim., Ser. A. 25*, 309–321.

Hastenrath, S. 1977b. Hemispheric asymmetry of oceanic heat budget in the Equatorial Atlantic and Eastern Pacific. *Tellus 29*, 523–529.

Hastenrath, S. and Lamb, P. J. 1977a. *Climatic atlas of the tropical Atlantic and Eastern Pacific Oceans.* University of Wisconsin Press.

Hastenrath, S. and Lamb, P. J. 1977b. Some aspects of circulation and climate over the Eastern Equatorial Atlantic. *Mon. Wea. Rev. 105*, 1019–1023.

Hantel, M. 1970. Monthly charts of wind vergence over the tropical Indian Ocean. *Bonner Meteorologische Abhandlungen 14*, 31–79.

Hantel, M. 1972. Wind stress curl—the forcing function for oceanic motions. In: *Studies of Physical Oceanography, tribute to George Wüst on his 80th birthday* (ed. A. C. Gordon), Vol. 1. New York and London: Gordon and Breach, pp. 121–136.

Jordan, C. L. 1951. Charts of the horizontal components of the mean surface wind over the oceans for January and July. *Bull. Am. Meteor. Soc. 32*, 375–379.

Koninklijk Nederlands Meteorologisch Instituut, 1918–31: Oceanographische en meteorologische waarnemingen in den Atlantischen Oceaan. Publication No. 11, four table volumes and one atlas volume.

Koninklijk Nederlands Meteorologisch Instituut, 1952: Indian Ocean oceanographic and meteorological data. Publication No. 135, 2nd ed., 2 vols.

Lamb, P. J. 1978. Case studies of Tropical Atlantic surface circulation patterns during recent Subsaharan weather anomalies: 1967 and 1968. *Mon. Wea. Rev. 106*, 482–491.

Lockwood, J. G., 1974. *World climatology; an environmental approach.* London: Arnold.

Mintz, Y. and Dean, G. 1952. The observed mean field of motion in the atmosphere. Geophys. Res. Papers No. 17, Air Force Cambridge Research Center, Cambridge, Mass.

Ramage, C. S. 1974. Structure of an oceanic near-equatorial trough deduced from research aircraft traverses. *Mon. Wea. Rev. 102*, 754–759.

Ramage, C. S., Miller, F. R. and Jefferies, C. 1972. *Meteorological atlas of the International Indian Ocean Expedition*, Vol. 1. U.S. Government Printing Office, Washington, D.C.

Romanov, Yu. A. and Romanova, N. A. 1976. Some results of the surface wind and atmospheric pressure fields analysis near the Equator. *Tellus 28*, 524–532.

Sadler, J. C. 1964. TIROS observations of the summer circulation and weather patterns of the Eastern North Pacific. Proc. Symp. Trop. Meteor., Rotorua, New Zealand Meteor. Service, 553–571.

Sadler, J. C. 1975. The monsoon circulation and cloudiness over the GATE area. *Mon. Wea. Rev. 103*, 369–387.

Saur, J. F. T. 1963. A study of the quality of sea water temperatures reported in logs of ships' weather observations. *J. Appl. Meteor. 2*, 417–425.

U.S. Navy, 1955–59. *Marine climatic atlas of the World.* Vols. 1–5. Chief of Naval Operation, U.S. Government Printing Office, Washington, D.C.

U.S. Weather Bureau, 1938. *Atlas of climatic charts of the oceans.* U.S. Government Printing Office, Washington, D.C.

Verploegh, G. 1967. Observation and analysis of surface wind over the ocean. Koninklijk Nederlands Meteorologisch Instituut, Mededelingen en Verhandelingen, No. 89.

О ДИНАМИКЕ И КЛИМАТОЛОГИИ ПОВЕРХНОСТНЫХ ТЕЧЕНИЙ В ЭКВАТОРИАЛЬНЫХ ОБЛАСТЯХ ОКЕАНОВ

С использованием судовых данных, осредненных за 60 лет, с разрешением по квадратам со стороной один градус исследуется циркуляция поверхностных вод в экваториальных областях Атлантики и восточной части Тихого океана. В середине лета в северном полушарии зонально ориентированный максимум скорости находится в восточных частях океанов около 4–5° с.ш. вблизи места, где течение через экватор меняет направление с юго-восточного на юго-западное. Оно разделяет полосу сильной дивергенции непосредственно к северу от экватора от пояса конвергенции далее к полюсам. Наиболее сильная конвергенция имеет место на 350 км южнее зоны сходимости пассатов северного и южного полушарий в области высокой устойчивости направления ветра. Отрицательное значение ротора напряжения ветра вызывает поднятие вод и низкие температуры поверхности моря непосредственно к югу от экватора и опускание вод к северу от него.

В большей части северо-восточных и юговосточных пассатов в южном полушарии в июле-августе диссипация энергии из-за трения, не подавляемая течением поперек изобар, приводит к постепениому замедлению течений и к конвергенции вниз по потоку. По мере того, как южные пассаты заходят за экватор, над восточными частями океанов ускорение Кориолиса увеличивается, действуя направо и увеличивая угол направления ветра к изобаре, что приводит к генерации кинетической энергии, к вышеупомянутому масимуму скорости и сопровождающей его зоне сильной дивергенции. Дальнейшее действие эффекта Кориолиса заворачивает поток с юго-восточного направления на юго-западное, что дальше вниз по потоку уменьшает угол к изобаре, подавляя таким образом генерацию кинетической энергии и приводя к появлению полосы максимальной конвергенции. Найдена положительная корреляция между положениями широты линии раздела северных и южных пассатов и широты интенсивности зонально ориентированных поясов конвергенции/дивергенции/как по сезонам, так и от года к году.